Na2-Mn[Fe(CN)6] Prussian blue analog cathodes for Na-ion batteries – From fundamentals to practical demonstration

Zhenying Li, Yu Wang, François Rabuel, Michael Deschamps, Gwenaëlle Rousse, Ozlem Sel, Jean-Marie Tarascon

$Na_{2-x}Mn[Fe(CN)_6]$ Prussian Blue Analog Cathodes for Na-ion Batteries – from fundamentals to practical demonstration

Zhenying Li,[1,2,3] Yu Wang,[1,2] François Rabuel,[2,4] Michael Deschamps,[5] Gwenaëlle Rousse,[1,2,3] Ozlem Sel[1,2,*] and Jean-Marie Tarascon[1,2,*]

[1] *Chimie du Solide et de l'Energie, CNRS, UMR 8260, Collège de France, 11 Place Marcelin Berthelot, F-75231 Paris Cedex 05, France*

[2] *Réseau sur le Stockage Electrochimique de l'Energie (RS2E), CNRS FR 3459, 33 Rue Saint Leu, F-80039 Amiens Cedex, France*

[3] *Sorbonne Université - 4 Place Jussieu, 75005 Paris, France*

[4] *Université de Picardie Jules Verne, Laboratoire de Réactivité et Chimie des Solides (LRCS), UMR 7314 CNRS, HUB de l'Energie, 80039 Amiens, France*

[5] *CNRS, CEMHTI UPR3079, Univ. Orléans, Orléans 45100, France*

Abstract: Prussian blue analogues (PBAs) hold significant promise as potential cathode materials for sodium ion batteries (SIBs) due to their various merits, such as large interstitial voids enabling efficient diffusive pathways, high theoretical capacity, ease of synthesis and lower cost. However, the structural water unavoidably generated during the synthesis significantly impacts the practical applications of PBAs. While it provides structural support, it can also undergo side reactions with sodium, compromising the stability and overall performance. To address this, we here in focus on the specific role of interstitial structural water in $Na_{2-x}Mn[Fe(CN)_6]_{1-y}\cdot\square_y\cdot nH_2O$ analogue, leading to the formation of hydrated H-NaMnHCF and dehydrated D-NaMnHCF. This allows us to elucidate the impact of interstitial structural water on the charge storage mechanisms in a comparative manner, using a combination of *ex situ* and *in situ* tools, including solid-state NMR, electrochemical quartz crystal microbalance (EQCM), and IR fiber-optic evanescent-wave-spectroscopy (IR-FOEWS). From this gained knowledge, we elaborated a processing protocol enabling the straightforward assembly of NaMnHCF 18650 cells using hard carbon (HC) anodes, demonstrating capacities of 548 mAh and high-rate capabilities (*72 % of initial capacity at 10C*). We believe that this contribution is of special interest to accelerate the commercial development of NaMnHCF PBA-based SIBs.

Keywords: Prussian blue analogues (PBAs), Na-ion batteries, sodium manganese hexacyanoferrate, Na-ion 18650 cell, *in-situ* analyses

1. Introduction

Several type of cathode materials including layered oxides, polyanionic compounds or Prussian blue analogues (PBAs) are currently proposed as cathodes for sodium-ion batteries (SIBs),[1, 2] while hard carbons (HC) are the most popular choice of anodes.[3] Among the cathode choices,[3] PBAs have emerged as compelling alternatives due to their relatively high theoretical capacity,[4] robust structural stability,[5] good rate capability,[6] and ease of synthesis.[7] PBAs have the general formula, $Na_{2-x}M'[M''(CN)_6]_{1-y}\cdot\square_y\cdot nH_2O$, where M' represents transition elements such as Mn, Fe, Co, Ni, Zn, while M" commonly denotes Fe. The symbol "□" signifies $[Fe(CN)_6]$ (hexacyanoferrate (HCF)) vacancies. Additionally, cost-effective synthesis methods, such as co-precipitation, further enhance the feasibility of commercial production.[8, 9]

Despite the many listed advantages that PBAs offer, and plans to develop the production of Na-ion cells based on PBAs, several issues need to be addressed for their full integration into practical applications, such as improving specific capacity and cycling stability. PBAs based on the M' site of Ni, Cu and Zn, namely Ni-HCF,[10] Cu-HCF,[11, 12] and Zn-HCF[13] possess only one electroactive site, *i.e.,* Fe, which leads to a lower theoretical capacity. Conversely, PBAs like Mn-HCF,[14] Fe-HCF[6, 15] and Co-HCF[16] feature two redox sites, resulting in a higher theoretical capacity. Mn-HCF stands out for its use of earth-abundant elements, enhancing cost-effectiveness in SIB production. $Na_{2-x}Mn[Fe(CN)_6]_{1-y}\cdot\square_y\cdot nH_2O$, the subject of this article, exhibits a higher average voltage, contributing to a superior energy density comparing to other PBAs. This composition, pioneered by Goodenough's group[17] for SIBs, has been a focus of research ever since, as further improvements were required.

One of the immediate improvements identified is the limitation of the number of $Fe(CN)_6$ vacancies in $Na_{2-x}Mn[Fe(CN)_6]_{1-y}\cdot\square_y\cdot nH_2O$. These defects are unavoidable during uncontrolled synthesis process and considerably reduce the capacity.[4] However, vacancies coordinated with water molecules (referred to as coordinated water) and located near $Fe(CN)_6$ octahedra have been shown to help maintain the structural stability, thereby enhancing the overall stability of PBAs.[18] Besides coordinated water, PBAs can host water in their structure in two additional ways: absorbed water and interstitial water. Firstly, water absorbed on the framework's surface has the potential to be released into the electrolyte. However, this issue can be circumvented by drying the electrode during preparation. Secondly, interstitial water within the interstitial space interact not only with Na^+ to create $Na(OH_2)^+$, but also forms hydrogen bonds with coordinated water molecules, requiring extreme dehydration conditions for its removal.[19] If not removed, interstitial water impedes Na^+ transfer, thereby reducing rate capability while leading to severe parasitic reactions.[20]

Consequently, the removal of coordinated and interstitial water is a critical processing issue which needs to be studied not only at the material level but also at the cell level for successful commercialization. Coordinated water poses relatively fewer issues due to the possibility of controlling its quantity by minimizing the number of $Fe(CN)_6$ vacancies during synthesis, and due to its relatively stable nature. These factors prompted us to revisit PBA's structure and composition, with a particular focus on interstitial water, as understanding this aspect is essential for preventing parasitic reactions during electrochemical cycling and for improving cathode handling during cell manufacturing. To gain insights into the interstitial water-electrochemistry relationship, we used *ex situ* and *in situ* tools, including solid-state NMR (SS-NMR),[21] Electrochemical quartz crystal microbalance (EQCM),[22] and IR fiber optic evanescent wave spectroscopy (IR-FOEWS).[23]

While numerous studies have explored PBA analogs in half-cells and full cells using coin cell formats,[24-26] their application in the 18650 format remains largely unexplored for this specific composition, with only two exceptions on other PBA analogs, [27]—one of which involves a research cell developed by a company.[18]

We then successfully met the challenge of implementing $Na_2Mn[Fe(CN)_6]\cdot zH_2O$ (hereafter denoted as NaMnHCF) as a PBA cathode in cylindrical 18650 format sodium ion cells, by developing a precise dehydration protocol for PBAs. To achieve this, we first refined a synthesis strategy to obtain a Na-rich structure with minimal number of defects via a simple precipitation method.[28] Next, through comprehensive structural, compositional and thermal analyses, we identified the conditions leading to hydrated H-NaMnHCF and dehydrated D-NaMnHCF (free of interstitial water), both of which have been studied to establish the structural water-electrochemistry relationship. The differing electrochemistry between H-NaMnHCF and D-NaMnHCF was demonstrated in half and full-cell configuration (*vs.* HC) in a coin cell format. In contrast to H-NaMnHCF//HC, D-NaMnHCF//HC exhibited a notable capacity and excellent cycling performance, provided that an optimized electrode drying protocol was applied. Building on this fundamental study, we have successfully implemented them in 18650 Na-ion cells, demonstrating that dehydrated PBAs are compelling cathode materials for SIB that require zero conflict minerals.

2. Results and discussion

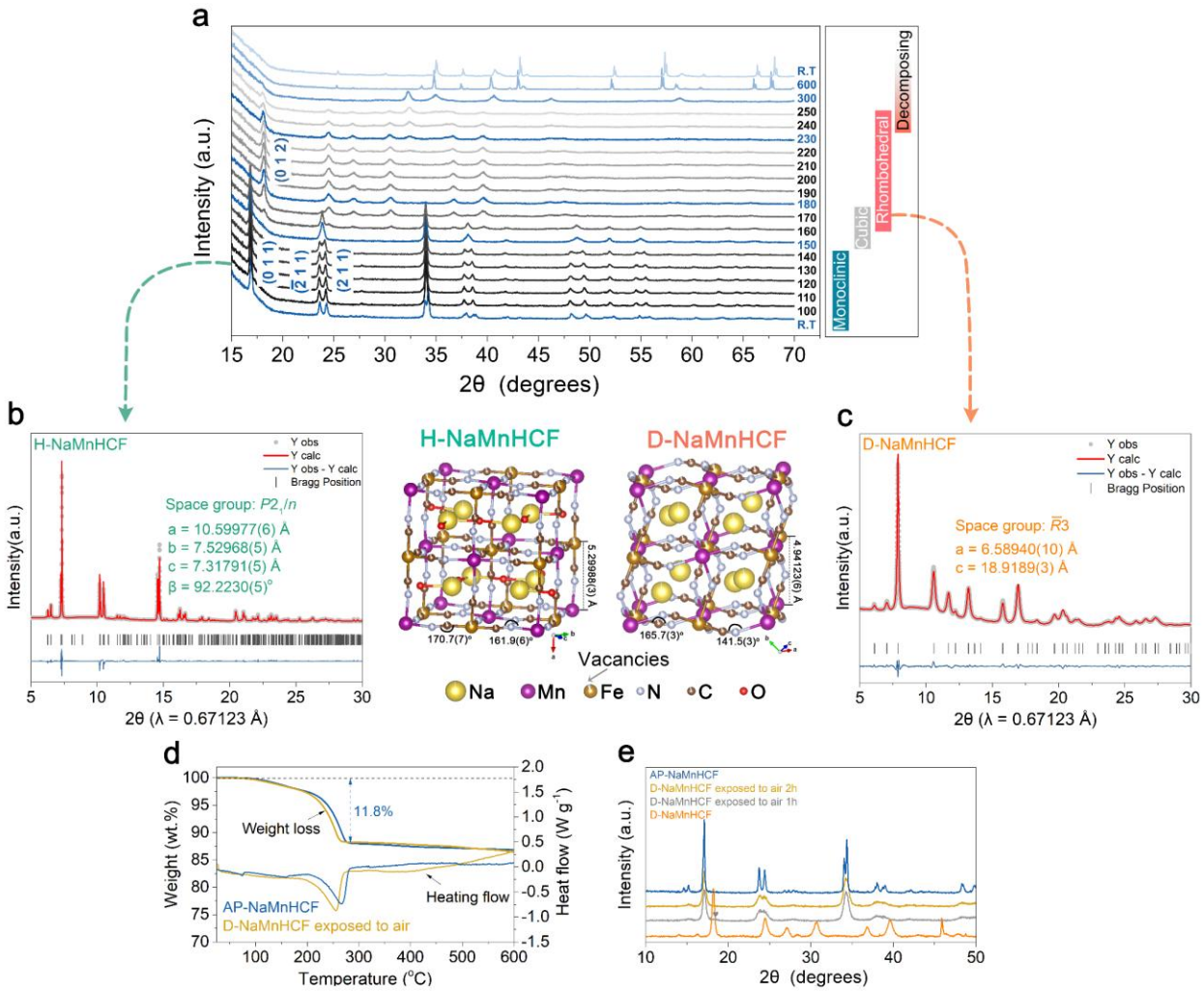

Figure 1. a. Temperature controlled XRD (TC-XRD, Cu-Kα radiation) of as-prepared material, AP-NaMnHCF. Rietveld refinements of the synchrotron X-ray diffraction patterns for **b.** H-NaMnHCF and **c.** D-NaMnHCF, along with schematic representations of the respective structural models. (The grey circles, red and blue continuous lines represent the observed, calculated and difference patterns, respectively. The vertical tick marks are Bragg positions). **d**. TGA-DSC analysis of AP-NaMnHCF and D-NaMnHCF exposed to air. **e**. XRD patterns of D-NaMnHCF powder and its evolution under air exposure, compared to that of AP-NaMnHCF (♥ indicates the presence of rhombohedral phase).

Characterization of AP-NaMnHCF powders: The synthesis of NaMnHCF powders with nominal chemical composition of $Na_2Mn[Fe(CN)_6]\cdot zH_2O$ was achieved *via* a co-precipitation method (see **Methods** for

details).[28] Inductively coupled plasma mass spectrometry (ICP-MS) (**Table S1**) and thermogravimetric analysis - differential scanning calorimetry (TGA-DSC) analyses (**Figure S1b**) allow us to deduce that AP-NaMnHCF adopts the molecular formula of $Na_{1.95}Mn[Fe(CN)_6]_{0.91}\square_{0.09} \cdot 2.22\ H_2O$. Furthermore, XRD pattern (**Figure S1c**) validates that the AP-NaMnHCF has a monoclinic structure with *P* $2_1/n$ space group, in agreement with the findings of Song *et al.*[24] All the characterization details can be found in the **Supporting Information**, **Part I** and in **Figure S1**.

Water loss/uptake mechanism: Temperature-controlled X-ray diffraction (TC-XRD) measurements were conducted to track dehydration process (**Figure 1a** and **S2**, under N_2 atmosphere to prevent material oxidation). AP-NaMnHCF exhibits a monoclinic phase from RT to 140°C. At 150°C, the merging of the $(\bar{2}11)$ and (211) peaks at approximately 2θ = 24° suggests the beginning of a monoclinic to cubic transition (**Figure 1a**). As the temperature continues to rise beyond 150°C, the cubic phase begins to transform into a rhombohedral phase. By 180°C, this transition is complete, with a single rhombohedral phase fully formed, indicating the end of the dehydration process. Decomposition initiates beyond 230°C. This sequence is similar to that of the NaFeHCF analog reported in the literature,[29-31] showing the same monoclinic to rhombohedral phase evolution, with the exception of a cubic intermediate phase observed here in NaMnHCF.

To monitor water content alongside phase evolution, TGA-DSC analyses were conducted over the same temperature range as TC-XRD (**Figure S1b**). At 80°C, absorbed water (1 wt%) removal begins, followed by the removal of interstitial water (11 wt%) which starts at 140°C, for a total loss of around 12 wt% by weight during the entire dehydration process. Stepwise isothermal TGA-DSC (**Figure S3**) also confirms this estimation. Overall, the structural and the thermal analyses enabled us to define the thermal treatment conditions for obtaining monoclinic H-NaMnHCF (100 °C), and rhombohedral D-NaMnHCF (175°C), with and without interstitial water, respectively.

To obtain H-NaMnHCF, AP-NaMnHCF was treated at 100°C under vacuum (10^{-2} bar), whereas obtaining D-NaMnHCF required a severe dehydration process conducted at 175 °C under strong vacuum conditions (10^{-6} bar). The crystal structures of these two samples were obtained from the Rietveld refinement of the synchrotron XRD patterns (**Figure 1b-c**), results are summarized in **Tables S2** and **S3**, and detailed elsewhere in literature (e.g. Ref.[24]). H-NaMnHCF exhibits a monoclinic phase with *P* $2_1/n$ space group with *a* = 10.59977(6) Å, *b* = 7.52968(5) Å, *c* = 7.31791(5) Å, β = 92.2230(5)°, whereas D-NaMnHCF exhibits a rhombohedral structure with *R* $\bar{3}$ space group with *a* = 6.58940(10) Å and *c* = 18.9189(3) Å. The crystal

structures are also illustrated in **Figure 1b-c** and further information is provided in the **Supporting Information**, **Part I.**

The compositions of the samples were determined through ICP-MS (**Table S1**), TGA and FTIR (**Figure S4a-b**). H-NaMnHCF is characterized by a molecular formula of $Na_{1.95}Mn[Fe(CN)_6]_{0.91\cdot\square 0.09} \cdot 2.01\ H_2O$. Upon removal of interstitial water, the resulting composition is represented by the molecular formula of $Na_{1.95}Mn[Fe(CN)_6]_{0.91\cdot\square 0.09} \cdot 0.08\ H_2O$. As shown in **Figure S4b**, no discernible peak corresponding to water was observed in D-NaMnHCF, suggesting that both absorbed and interstitial water were effectively removed from the structure, while coordinated water was not detected due to its limited amount (*i.e.,* $Na_{1.95}Mn[Fe(CN)_6]_{0.91} \cdot 0.08\ H_2O$). However, the D-NaMnHCF can quickly re-absorb water under ambient conditions converting back to AP-NaMnHCF, as confirmed by TGA-DSC (**Figure 1d** and **S5**) and XRD (**Figure 1e**). Overall, thermal treatment along with the structural analysis reveal that the phase transitions of NaMnHCF, from rhombohedral to monoclinic is driven by the presence/absence of interstitial water, or vice versa. This finding aligns with the observations reported by Maddar *et al.*[29]

Electrochemical Analysis: First, we examined the electrochemical behavior of the H-NaMnHCF and D-NaMnHCF based cathodes in half-cell configuration (see **Methods**). The electrochemical behavior of H-NaMnHCF and D-NaMnHCF was tested at a current rate of C/10 against Na in coin cells using 1M $NaPF_6$ in propylene carbonate (PC) as electrolyte. H-NaMnHCF (**Figure S6a-b**) shows a stair case voltage variation during the 1st charge, which disappears on subsequent charges to give an overall reversible capacity of 139 mA h $g^{-1.}$ This contrasts with D-NaMnHCF that shows a single voltage charge-discharge plateau corresponding to a reversible capacity of 157 mA h g^{-1} (**Figure S6c-d**). In terms of cycling stability, their performance seems to be similar up to the 50th cycles, after which the performance difference appears in favor of D-NaMnHCF (**Figure S7a**). Furthermore, it should be noted that D-NaMnHCF outperforms H-NaMnHCF in terms of rate performance (**Figure S7b**). D-NaMnHCF shows a notable capacity at 30C (~100 mA h g^{-1}), whereas the H-NaMnHCF already shows a significant capacity loss at 5C. This difference can be explained by structural considerations, with D-NaMnHCF exhibiting the larger empty interstitial voids to facilitate ions transfer.

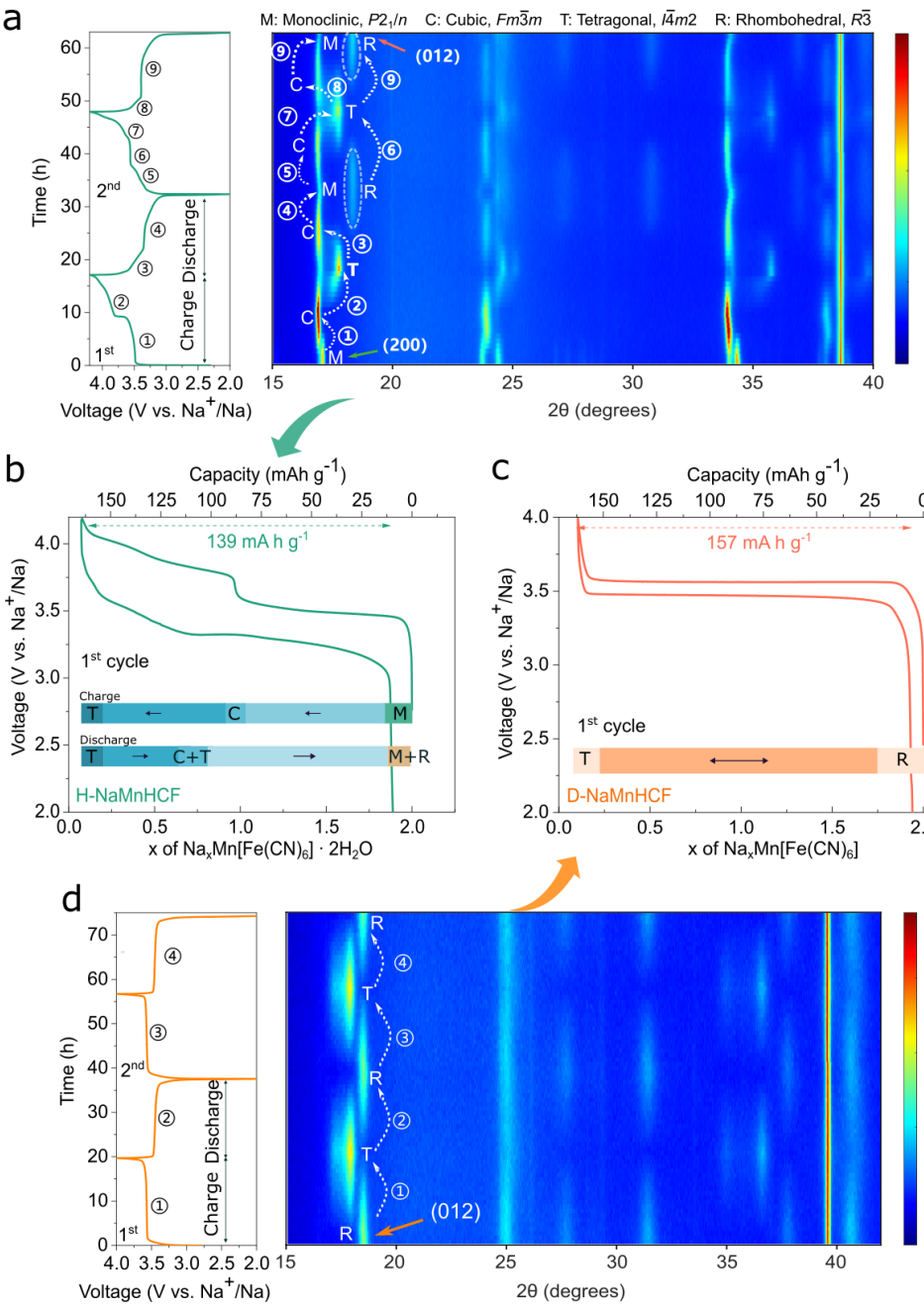

Figure 2. Sodium ion (de)intercalation mechanism and structural changes monitored by *in-situ* XRD for two cycles. **a** and **b.** H- NaMnHCF and **c** and **d.** D- NaMnHCF (simplified compositions were used for clarity). Galvanostatic charge and discharge (GCD) curves are taken at C/17 and C/20 in 1M $NaPF_6$ in PC, respectively. Middle panels (**b** and **c**) show the GCD curve and the corresponding phase evolutions, for clarity only first cycle is shown, refer to **Figure S9** for the second cycle. XRD color bar: blue (low intensity) to red (high intensity).

Next, to explain the different voltage profiles observed for H-NaMnHCF and D-NaMnHCF *in-situ* XRD measurements were carried out during the first two cycles and the collected XRD patterns are reported in **Figure 2** and **S8**. During the first charge of H-NaMnHCF, when the 1st Na^+ ion is removed from the framework through the first plateau (**Figure 2a-b**), the phase evolves from monoclinic to cubic. When the 2nd Na^+ is removed during the upper plateau, the structure evolves from cubic to tetragonal. During the following discharge, the tetragonal phase reconverts into a cubic phase, which then transforms into monoclinic phase after further Na^+ insertion (**Figure 2a**, 4) which coexists with minor amount of rhombohedral phase suggesting that part of the interstitial water has partially been removed from the structure. During the second charge, the phases evolve according to the sequence (**Figure 2a**, 5-7): monoclinic to cubic, then rhombohedral to tetragonal, and finally cubic to tetragonal. Finally, phase evolution through the second discharge early mirrors that observed during the first discharge. Similar processes also reported and detailed elsewhere in literature (e.g. Ref.[24]). However, it should be noted that after the second cycle, the intensity of the monoclinic phase peak (200) decreases, while the rhombohedral phase peak (012) becomes more prominent than towards the end of first cycle, implying the gradual elimination of interstitial water upon subsequent cycling (**Figure S8b**).

In contrast, *in-situ* XRD for D-NaMnHCF show a phase transition from rhombohedral to tetragonal during charging that occurs in the opposite direction during the subsequent discharge (**Figure 2c-d** and **S8c-d**), confirming the reversibility of the Na^+ uptake-removal process in line with the electrochemical data. All phase evolution details were well explained in **Figure S8** and **S9**. Thus, *in-situ* XRD clearly confirms that the difference in voltage profile between first charge and discharge observed for H-NaMnHCF is due to differences in the structural evolution of the phases, probably as the result of the partial loss of structural water during sodium extraction from H-NaMnHCF.

To further substantiate the interstitial water removal during the charge of the H-NaMnHCF cathode, we performed EQCM analysis (**Figure S10**-**S11**). H-NaMnHCF spray-coated quartz resonators were assembled in a battery EQCM cell, with Na metal serving both reference and counter electrodes and 1M $NaPF_6$ in PC as electrolyte (see **Methods**). The mass variation (Δm) of H-NaMnHCF during charge in a cyclic voltammetry (CV-EQCM) mode, at 0.1 mV s^{-1} between 2.5 and 4 V *vs.* Na/Na^+ is shown in **Figure S10a**. The first charge of H-NaMnHCF shows two redox peaks that are associated to masses per electron (MPE) of 43 g mol^{-1} (*n*: ~1.0) and 54 g mol^{-1} (*n*: ~1.7) for region I and II, respectively (**Figure S10b**). This is consistent with TGA analysis on the half-charged H-NaMnHCF sample that reveals a total mass loss of ~6% corresponding to the removal of nearly one water molecule ($Na^+.H_2O$ (41 g mol^{-1})) (**Figure S12**). In contrast, a M.P.E. value of

solely 24 g mol^{-1} ($Mw_{(Na^+)}$: 22.98 g mol^{-1}) was measured for D-NaMnHCF sample (**Figure S10c** and **d)** implying the removal of bare Na^+ only.

The outcome of water upon electrochemical oxidation was further explored by *ex-situ* SS-NMR. The ^{23}Na SS-NMR spectra for D-NaMnHCF (**Figure 3a**) displays a single peak (initially at 120.3 ppm, **Figure 3a,** 1) with very little spinning sidebands indicating a symmetric environment and small quadrupolar interaction for Na^+ ions in the rhombohedral phase. Upon charging, a broad shoulder at lower ppm is detected in the ^{23}Na spectrum of the half-charged sample (**Figure 3a**, 2), which we believe to be associated with the appearance of the tetragonal phase. In accordance with electrochemistry (**Figure 2c**), no sodium ions are detected in the charged sample (**Figure 3a**, 3) by SS-NMR. The discharge process is quite reversible, although a slightly more visible shoulder is detected in the 40 to -30 ppm range (**Figure 3a,** 4) that may correspond to sodium ions populating the tetragonal phase before recreating the initial rhombohedral phase during discharge. The final peak at the end of the discharge is very similar to the initial one, confirming the reversibility of the process (**Figure 3a,** 4).

For monoclinic H-NaMnHCF (**Figure 3b**), the ^{23}Na SS-NMR spectra is more complex. The pristine phase (**Figure 3b,** 1) shows Na^+ ions in a single environment, peak at around 20 ppm, with the spinning sidebands stemming from a larger quadrupolar interaction indicating that the local environment of sodium is markedly less symmetric than for rhombohedral D-NaMnHCF. Upon charging, 1^{st} Na^+ ions are removed, but no further signal is detected (**Figure 3b,** 2), implying that, despite a phase change from monoclinic to cubic (**Figure 2a,** 1 and **2b**), the sodium ion environment remains unchanged. During the next discharge, some sodium atoms reappear in the original environment (around 20 ppm) and others in a broad peak centered around 80-100 ppm (**Figure 3b,** 4). Nevertheless, at full discharge, 50-60% of the sodium ions are found around 120 ppm, in an environment close to that found for D-NaMnHCF (**Figure 3a**) with the remaining 40-50% are sitting in a more disordered environment (~50 ppm), most likely due to the irreversible transformation triggered by the removal of water (**Figure 3b,** 5). After the second discharge the ^{23}Na environment is similar to that observed after the first discharge implying a nearly reversible process, once the first charge has been completed (**Figure 3b,** 6).

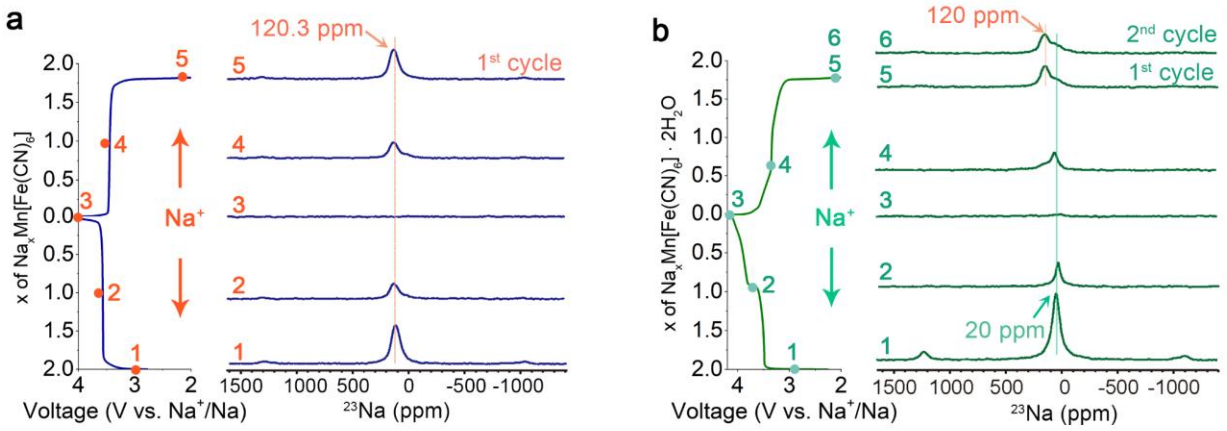

Figure 3. *Ex-situ* ^{23}Na SS-NMR spectra (right hand-side figures) of **a.** D-NaMnHCF and of **b.** H-NaMnHCF. The samples' collected state was also marked in the GCD curves (left hand-side). The GCD tests were carried out at C/20 in 1M $NaPF_6$ in PC. The state marked as (6) in H-NaMnHCF (b) corresponds to samples which have been cycled twice and collected at the end of the second discharge step.

Interestingly, the ^{1}H SS-NMR spectrum shows that hydrogen atoms are detected around ~4.5 ppm (close to the H_2O shift), in the form of a broad peak (linewidth around 30 ppm, with a broad shoulder on the left-hand side), indicating reduced proton mobility (**Figure S13**). During charging, the peak (72% of the initial signal area) appears displaced at 0 ppm at mid-charge and becomes much narrower (linewidth 8 ppm), indicating that proton mobility has increased. At full charge, besides a peak at -2 ppm, and a group of resonance is detected at 4.4 ppm, while a broad shoulder is still detected on the left-hand side, extending to 10 ppm. Interestingly, towards the middle of the first discharge these various peaks disappear to the expense of a single intense peak around -1 ppm (width around 7 ppm) which further evolves into a broad peak (very similar to the initial state 1, **Figure S13**) surmounted by a narrower peak at ~4.5 ppm but with additional shoulder on the right-hand side. This suggests that Na^+ removal-uptake is not totally reversible, with the observed shoulder most likely highlighting the creation of new environments, potentially stemming from the reactivity of the de-sodiated phase with the solvent (**Figure S13**, 5 and 6 ☆). Overall, the ^{1}H SS-NMR data indicates a greater proton mobility for charged or discharged samples, indicating that H_2O removal becomes easier from H-NaMnHCF once sodium removal has been initiated electrochemically, in agreement with a previous literature report in Ref. [32].

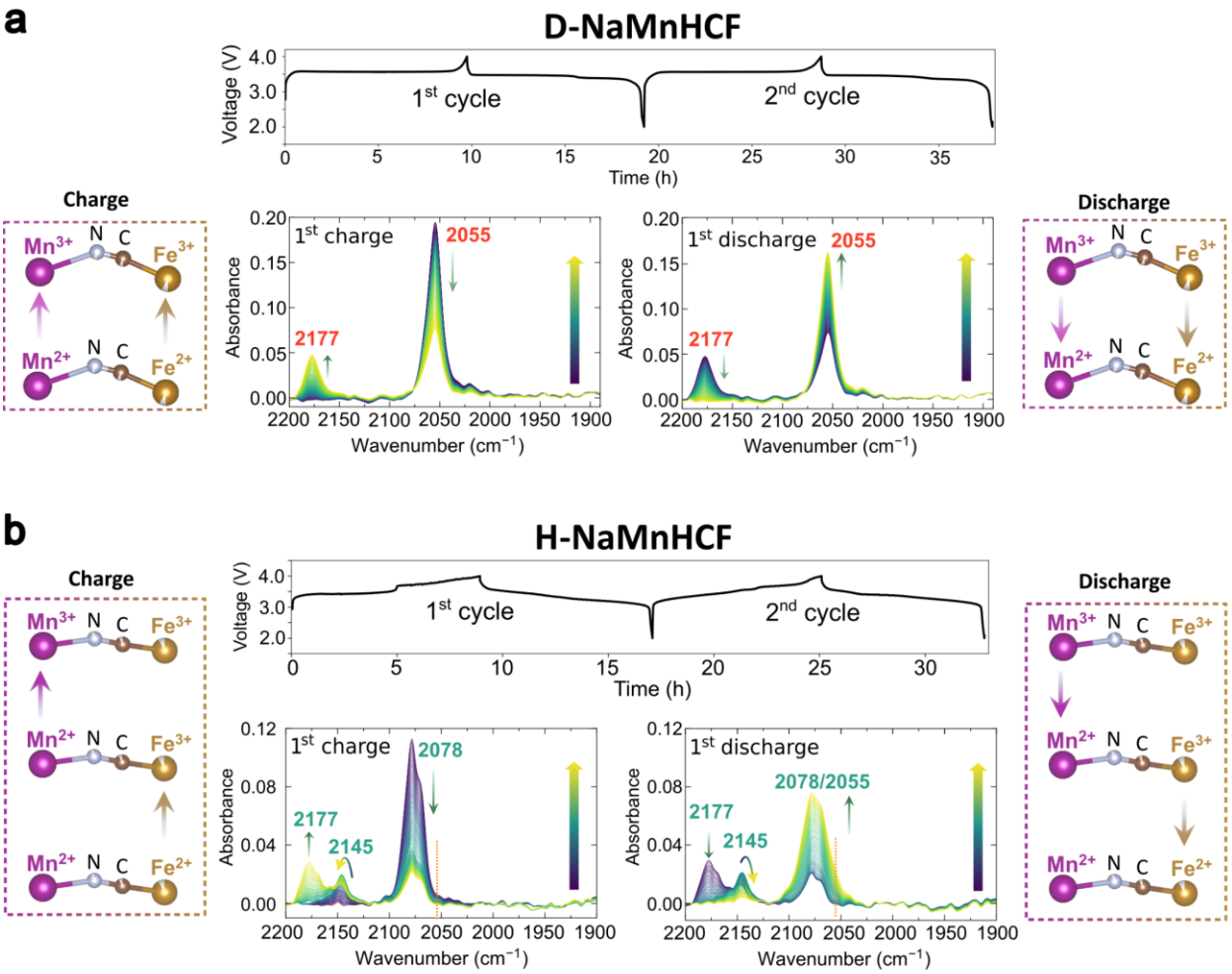

Figure 4. *Operando* IR-FOEWS measurement of fiber coated and embedded in **a.** D-NaMnHCF and **b.** in H-NaMnHCF cathodes and cycled in 1M $NaPF_6$ in PC versus Na as anode. The upper panels in (a) and (b) are the first two galvanostatic charge-discharge patterns whereas the lower panels present the simultaneously obtained IR spectra, focusing in the ν-CN absorbance region shown for the 1st charge and 1st discharge process. Color bar represents the process from beginning (dark purple) to end (green).

Then, on the basis of previous reports showing that the ν-CN stretching band is highly sensitive to Na-driven structural changes in PBAs phase[33], we carried out IR operando fiber optic evanescent wave spectroscopy (IR-FOEWS) on the D-NaMnHCF and H-NaMnHCF system using an in-house developed technique.[23] It consists in placing IR-transparent chalcogenide fibers ($Te_2As_3Se_5$ (TAS)) in our active electrode material and collecting spectra over the 800-7000 cm^{-1} wavelength domain during cell charging or discharging while mainly focusing on monitoring the ν-CN stretching band.[33] The IR spectra recorded during the charging-discharging of Na//D-NaMnHCF and Na//H-NaMnHCF half cells are shown in **Figures 4a** and **4b**, respectively.

For the Na//D-NaMnHCF cell (**Figure 4a**), a continuous decrease of the ν-CN absorbance band at 2055 cm^{-1} at the expense of a new one at 2177 cm^{-1} is observed upon Na^{+} removal (and vice versa during discharging). This evolution, consistent with a two-phase process, can be explained in accordance with the literature on the basis of the relative redox energy levels of the two electrochemically active cations (Fe and Mn). Their positioning is governed by competing ionization energy (low Fe^{2+}/Fe^{3+} redox potential) and ligand field stabilization energy (LFSE) (high Fe^{2+}/Fe^{3+} redox potential) considerations.[34] When these different energy terms for Fe^{2+}/Fe^{3+} and Mn^{2+}/Mn^{3+} balance each other, the oxidation process of D-NaMnHCF cell occurs via single phase plateau.[34]

In contrast, the IR spectra recorded for the Na//H-NaMnHCF, having two plateaus in charge, shows a different evolution of the ν-CN-absorbance (**Figure 4b**). Upon charge, through the first plateau, the absorbance band at 2078 cm^{-1} decreases at the expense of that at 2145 cm^{-1} that increases with the appearance of a new band at 2177 cm^{-1} on reaching the second plateau. This is consistent with the chemical environment of ν-CN, which differs from that of D-NaMnHCF. In the presence of interstitial water, the balance between the competing effects of ionization energy and LFSE for Fe and Mn is disrupted. This results in the appearance of an energy difference between the Fe^{2+}/Fe^{3+} and Mn^{2+}/Mn^{3+} redox potentials, leading to two plateaus in the charge voltage profile curve (**Figure 4b**). During the following discharge, we observe an almost inverse evolution of the IR spectra, with the emergence of a shoulder at the 2055 cm^{-1}, indicating a partial "irreversible transformation" upon water removal, in agreement with the findings of the *ex-situ* ^{23}Na SS-NMR (**Figure 3**).

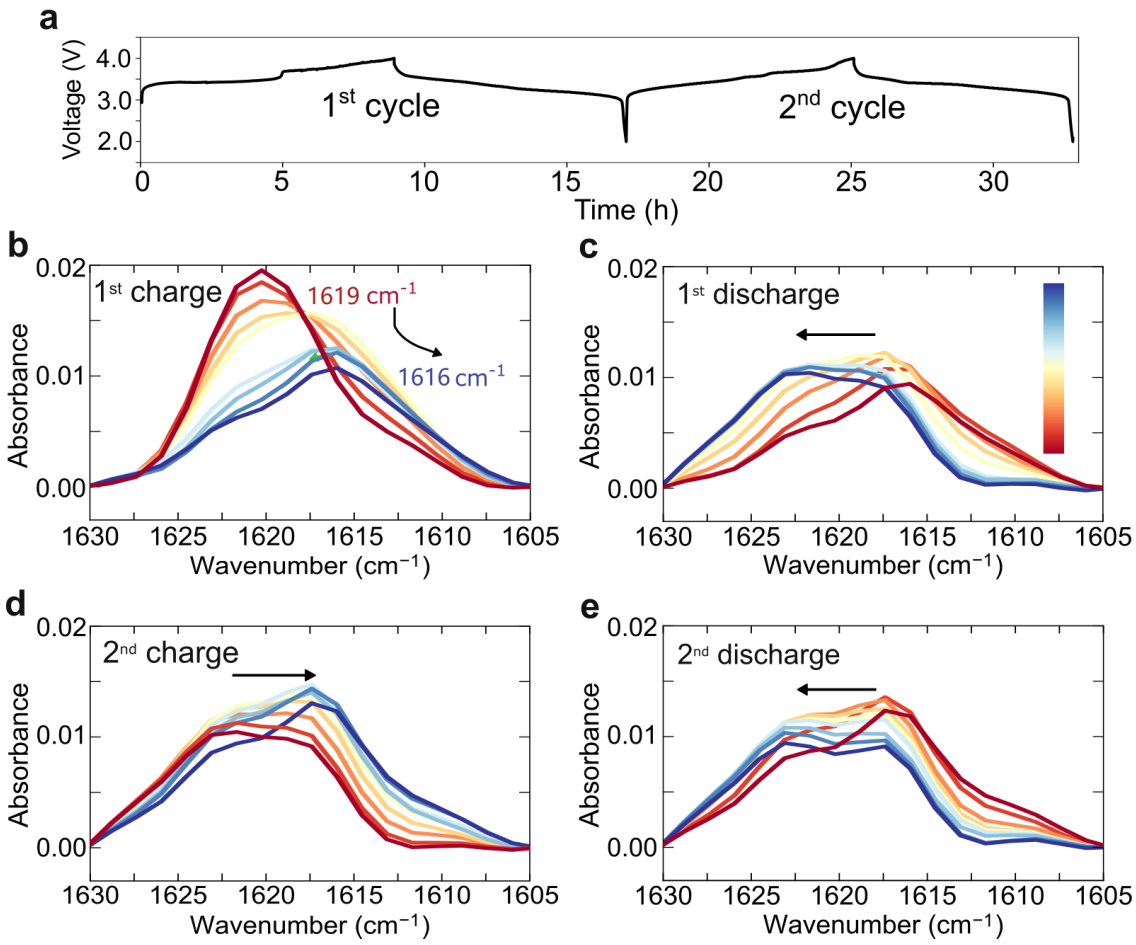

Figure 5. *Operando* IR-FOEWS measurement of fiber coated with and embedded in H-NaMnHCF cathodes in 1M $NaPF_6$ in PC. **a**. The first two GCD patterns and the lower panels (**b**-**e**) present the simultaneously obtained IR spectra, focusing in the ν-OH absorbance region. **b**. 1st charge, **c**. 1st discharge, **d**. 2nd charge and **e**. 2nd discharge. Color bar represents the process from beginning (red) to end (blue).

We were also able to follow the evolution of the ν-OH bending vibration (**Figure 5b**) and found that the initial absorbance at 1619 cm^{-1} decreases in intensity and shifts to 1616 cm^{-1} upon charging. The irreversible absorbance decrease confirms interstitial water removal, while the red shift suggests that, upon Na^+ extraction, the remaining interstitial water forms stronger H-bonds, lowering the bending mode frequency.[24] During discharge, the ν-OH bending peak shifts back at 1619 cm^{-1} indicating weaker H-bonds due to their re-orientation around the inserted Na^+ ions (**Figure 5c**). The near constancy of the amplitude of the ν-OH peak, which oscillates between 1619 cm^{-1} to 1616 cm^{-1} during the second cycle and upon subsequent cycle when the Na^+ ions are extracted/inserted (**Figure 5d** and **e**), suggests that partial water removal occurs mainly during the first charge and barely evolves afterwards. Therefore, achieving the same state of water

content in H-NaMnHCF through cycling will never be identical to that in thermally treated D-NaMnHCF. This discrepancy is likely linked to the different process drivers: during heat treatment, thermal energy is more efficient at thoroughly removing interstitial water, whereas electrochemical water removal, primarily associated with Na^+ extraction, is less effective, leaving residual interstitial water within the framework.

Next, we explored the performance of these electrodes in complete PBA//HC cells. We first assembled 2032-type coin cells using H-NaMnHCF and D-NaMnHCF as cathodes, paired them with Hard carbon (HC) anode in presence of 1M $NaPF_6$ in PC electrolyte (**Figure S14a**). The assembled H-NaMnHCF//HC cell shows an initial charge capacity of 135 mAh g^{-1} at C/10, of which only 18 mAh g^{-1} can be recovered during discharge (**Figure S14b**). This come as a surprise since this material could be cycled versus Na metal. To understand this difference, we dismantled the coin cell and recovered the "discharged H-NaMnHCF" which was then cycled in a second coin cell against Na metal. The cell was initially charged and barely no capacity was obtained implying the absence of Na^+ in the recovered discharged positive electrode, suggesting the presence of parasitic reactions capturing Na-ion (**Figure S14c**). A more severe deterioration was observed in the recovered HC anode, since only 65% of the initial capacity was recovered (**Figure S14d** and **S15**). Possible reasons for the irreversible decrease in HC performance could be related to side products of the parasitic reactions (see Supporting Information for details)—namely, NaOH and HF—and its effect on the hard carbon surface (**Figure S15**). We believe that the recovered electrodes' behavior is due to the water electrochemically removed from the H-NaMnHCF during charging, which reacts with Na/electrolyte and in the absence of Na reservoir, not enough Na remains to fully sodiate H-NaMnHCF phase during full cell's discharge. The same situation occurs with Na-half cells, with the difference that, owing to the large excess of Na (use of Na metallic foil at the negative electrode), cycling can proceed for quite sometimes. Thus, H-NaMnHCF cannot be directly used for practical applications in full cell configuration.

Conversely, the Na-ion D-NaMnHCF//HC cell (**Figure 6a**) shows charge/discharge capacities of 149 and 125 mA h g^{-1} at C/10, with an initial coulombic efficiency of 84% (**Figure 6b**). Subsequently, the cell also exhibits good reversibility and cyclability, so that it can still deliver 70% of its initial capacity after 200 cycles at 25°C. (**Figure 6e**). Moreover, the signature curve shows that the full cell delivers excellent capacities of 124, 123, 121, 117, 110, 92, 41 mA h g^{-1} at C/20, C/10, C/5, C/2, 1C, 2C, 5C, respectively (**Figure 6d**).

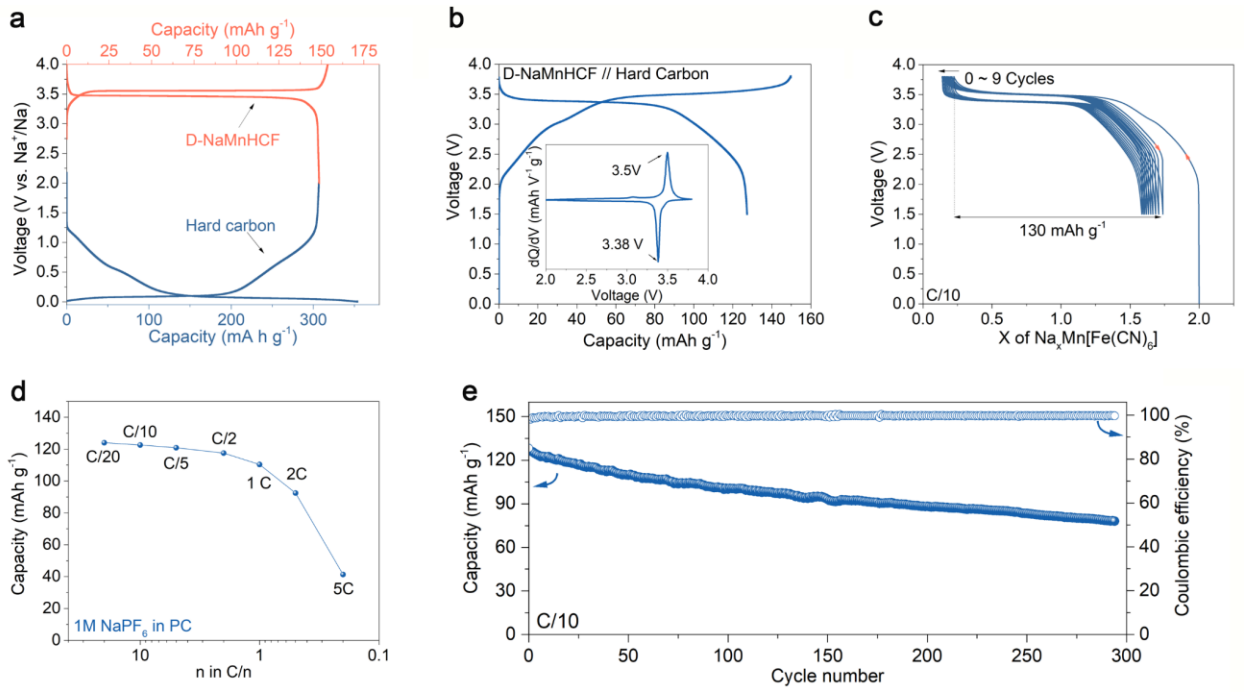

Figure 6. The initial galvanostatic charge/discharge curves of D-NaMnHCF *vs.* Na^+/Na and HC *vs.* Na^+/Na, **b.** full cell test of D-NaMnHCF//HC first cycle, **c.** Na^+ insertion/extraction shown for the first 10 cycles, **d.** the rate capability between C/20 and 5C and **e.** the cycling stability of the D-NaMnHCF versus HC, carried out at 0.1 C in 1M $NaPF_6$ in PC in coin cells.

Both this rate performance and long-term cycling stability prompted us to explore the making of Na-ion 18650 cells based on the D-NaMnHCF//HC chemistry, as we shall see next. An inherent obstacle to processing D-NaMnHCF is that it readily reabsorbs water from the surrounding environment to transform into H-NaMnHCF (**Figure 1 d-e** and **S5**), hence the need to process this material (storage + handling) in a moisture-free environment (*e.g.* a dry room). To partially overcome this problem, we exploited the possibility of making the jelly roll composed of the H-NaMnHCF//HC pair and dehydrate it just before electrolyte filling in the 18650 cells (see **Methods**), but our approach failed because of our separator (ceramic-coated polypropylene (PP) separator) could not sustain dehydration temperature of 150°C under vacuum while preserving its porous structure (**Figure S16**). We therefore ended up following a protocol 2, in which H-NaMnHCF was cast onto Al current collectors and dehydrated (150°C under vacuum) to obtain D-NaMnHCF supported on Al foils (**Figure 7a**), followed by further characterization (**Figure S17-18**). Dehydration temperature was adjusted for composite electrodes compared to pristine powder.[29] The as fabricated positive electrode was wound with PP ceramic separator and hard carbon-supported Al foil in the dry room to obtain a jelly roll that was inserted into 18650 cell cans.

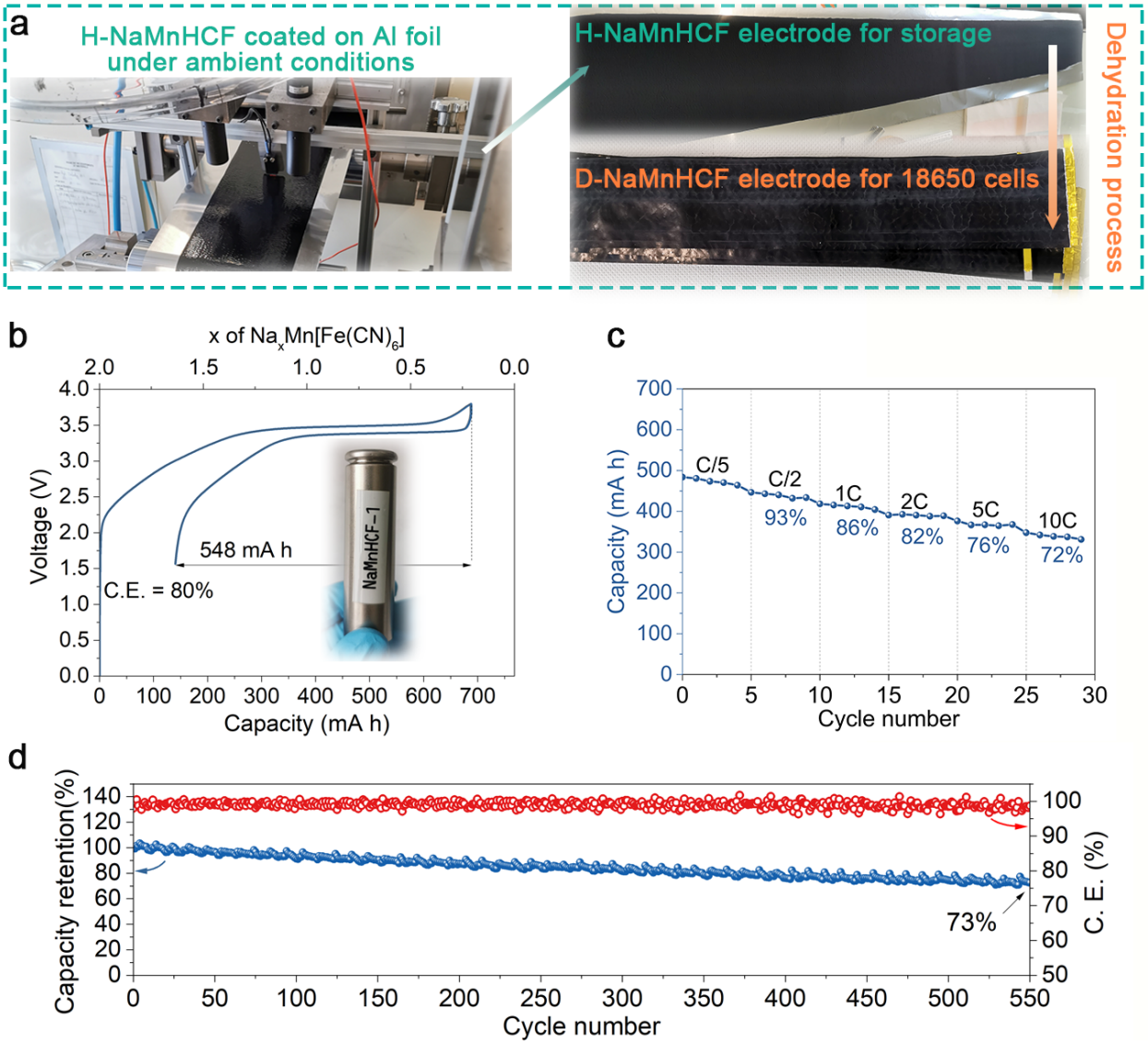

Figure 7. 18650 cell fabrication of D-NaMnHCF//HC and the analysis of the cathode electrode. **a.** Coating of H-NaMnHCF on Al current collector under ambient conditions, **b.** the formation cycle of the D-NaMnHCF//HC 18650 cell at C/20, **c.** the rate performance and **d.** cycling performance at C/2 of the cell**.** The cathode composition is as follows: active material: C_{sp}: PVDF = 71%: 22.5%: 6.5%. The cathode mass loading is ~ 15 -16 mg cm^{-2}, and the anode mass loading of ~ 5-6 mg cm^{-2}. All the tests are done in 1M $NaPF_6$ in EC: PC: DMC at 25°C. C.E. refers to coulombic efficiency.

The assembled 18650 cells containing a 1M $NaPF_6$ EC/PC/DMC electrolyte (**Figure S19**) were electrochemically tested using constant current, constant voltage (CCCV) protocol detailed in the **Methods** part. They deliver a capacity of 687 mA h in charge and 548 mA h in discharge (**Figure 7b**) with this capacity

still equal to 73% of its initial capacity at C/2 after 550 cycles (**Figure 7d**). Concerning the rate performance, capacities of 474, 439, 409, 387, 363, 340 mA h can be achieved at rates of C/5, C/2, 1C, 2C, 5C, 10C respectively (**Figure 7c**), thus keeping the 72 % of the initial capacity from C/5 to 10C. This power rate capability is best represented by the Ragone plot for D-NaMnHCF versus HC 18650-type cells in **Figure S20** (normalized by the total mass of cathode and anode), which shows an energy density of 125 Wh kg^{-1} at power density of 40 W kg^{-1} and 68 Wh kg^{-1} at power density of 1140 W kg^{-1}, respectively. To the best of our knowledge, only two 18650 cell prototypes incorporating PBAs have been reported in the literature. One uses NaFeHCF and the other NaFeMnHCF with a HC anode, in 1M $NaBF_4$ in tetraglyme and 1M $NaPF_6$ in diethylene glycol dimethyl ether, respectively. Although the conditions are not identical, for comparison purposes, we benchmarked our results against these two recent studies in terms of capacity, rate performance and cycling stability. Our cells present an intermediate capacity of 548 mAh, compared to the work of Chou *et al.*[18], which achieved 700 mAh in NaFeMnHCF//HC cells, and Balaya *et al.*[35], which achieved 450 mAh in NaFeHCF//HC cell. By comparing to the higher capacity cell,[18] the difference is simply due to the 1.2 times more mass loading that can be closed by further optimizing our electrodes dry masses. Although not yet optimized, our current 18650 cell shows notable rate capability with 78% of nominal capacity retained at 5C, compared with 50% at 4C and 62% at 2C for NaFeMnHCF//HC [18] and NaFeHCF//HC [35], respectively. Future developments will include optimizing the PBA cathode with a larger particle size to increase the tap density while maintaining the electronic conductivity at an appropriate level, as well as refining the electrolyte composition.

Conclusions

We have reported on the impact of interstitial water in the Prussian Blue analog NaMnHCF phase, synthesized with a Na-rich structure with minimal number of defects and investigated by combining XRD, TGA, EQCM, SS-NMR and IR-FOEWS techniques. Using TC-XRD and TGA-DSC, we followed the phase evolution and water loss mechanism during the dehydration process, enabling us to precisely control the conditions for obtaining the pure hydrate and dehydrate forms of NaMnHCF. We revealed that the phase transitions of NaMnHCF, from rhombohedral to monoclinic, are driven by the presence or absence of interstitial water. Most importantly, we observed using a panel of *ex-situ* and *in-situ* tools that the structural water in H-NaMnHCF is at least partially removed from interstitial voids during charging. It has been shown that the eliminated water leads to parasitic reactions that consume Na, impairing the performance of Na-ion H-NaMnHCF cells and rendering this phase unusable for practical applications. In contrast, we showed that

full Na-ion cells based on the D-NaMnHCF//HC chemistry exhibit a good cycling performance of 125 mA h g^{-1} at C/10 with 70% of this capacity being maintained till 200 cycles. Finally, this systematic study has enabled us to identify a precision dehydration protocol for PBAs to obtain high-performance Na-ion 18650 cells with capacities of 548 mAh and high rate capabilities (*72 % of initial capacity at 10C*). We anticipate that the established processing protocol supported by the key parameters provided by our fundamental study, will accelerate the full integration of NaMnHCF PBA-based SIBs into commercial developments.

Methods Section

Materials. All the chemicals were purchased commercially and used without further purification. Sodium ferrocyanide decahydrate ($Na_4Fe(CN)_6 \cdot 10H_2O$, ≥ 98.0%, Sigma-Aldrich), Trisodium citrate dihydrate ($Na_3C_6H_5O_7 \cdot 2H_2O$, 99.0%, Thermo Scientific Chemicals), Sodium chloride (NaCl, 99,5 %, Thermo Scientific Chemicals) and Manganese(II) chloride tetrahydrate ($MnCl_2 \cdot 2H_2O$, ≥99%, Sigma-Aldrich) were used for the PBA synthesis. $NaPF_6$, propylene carbonate (PC), ethylene carbonate (EC) and dimethyl carbonate (DMC) were purchased from Dodochem. N-Methyl-2-pyrrolidone (NMP) was acquired from Sigma-Aldrich. Hard Carbon (HC) electrode and powder are provided from Tiamat Company, France.

Synthesis of NaMnHCF. NaMnHCF compound was synthesized by using a co-precipitation method.[28] First, 35.9 mmol $Na_4Fe(CN)_6 \cdot 10H_2O$, 142.8 mmol $Na_3C_6H_5O_7 \cdot 2H_2O$ and 7.2 mol NaCl were dissolved together in 1.125 L deionized water. Then, the co-precipitation reaction was performed at room temperature by dropwise addition of 71.5 mmol $MnCl_2 \cdot 2H_2O$ into 500 mL deionized water. The whole process was performed in a continuous stirred tank reactor (CSTR, Eppendorf BioFlo 320) with a stirring speed of 1,000 rpm and a solution adding speed of 0.2 mL min^{-1}. Next, the precipitate was aged overnight and then washed with deionized water and ethanol for several times and denoted as AP-NaMnHCF. Finally, the D-NaMnHCF was obtained by drying at 175 °C for 20 h in a specific vacuum pressure of 10^{-6} bar. For comparison, the H-NaMnHCF was obtained by drying it in a vacuum oven (10^{-2} bar**)** at 100 °C for 10 h.

Materials characterization. X-ray diffraction (XRD), including *in-situ* experiment during electrochemical cycling, was performed using a laboratory X-ray diffractometer (Bruker D8 Advance) equipped with a Cu Kα radiation source ($\lambda_{K\alpha1}$ = 1.54056 Å, $\lambda_{K\alpha2}$ = 1.54439 Å) and a Lynxeye XE detector. A homemade airtight cell with Beryllium window was used. Temperature-controlled X-ray diffraction measurements on NaMnHCF powder was carried out from room temperature (R.T.) up to 600 °C, under N_2. The same Bruker D8 diffractometer introduced above, but equipped with a HTK 1200 °C Anton Par Chamber, was used to perform

such measurement with a heating rate of 5 °C min^{-1}. All the XRD curves were recorded for approximately 1h at a constant temperature between 2θ = 10° and 2θ = 70°. Synchrotron XRD measurements were conducted at the CRISTAL beamline (λ = 0.67123 Å) at synchrotron SOLEIL in France. The experiments were carried out in transmission mode, with samples placed in borosilicate capillaries (0.7 mm in diameter) in a glove-box and sealed. Rietveld refinements were performed using the FullProf program. Thermogravimetric analysis with differential scanning calorimetry (TGA-DSC) was performed using a Mettler-Toledo TGA-DSC STARe system. Alumina crucible was loaded with 15 – 20 mg of powder sample and experiment was run between R.T. and 600 °C ramped at 5 °C min^{-1} in a constant flow of dry Ar gas. Fourier-transform Infrared spectroscopy (FTIR) was performed using Nicolet Summit FTIR Spectrometer in Ar-filled glovebox. Inductively coupled plasma mass spectrometry (ICP-MS) was performed using a PekinElmer NexION 2000 ICP mass spectrometer. The sample powder was dissolved in an acidic solution (5 % H_2SO_4, 5% H_2O_2, 90% deionized water) and then diluted with 2 v/v % HNO_3 in a volumetric flask to the appropriate concentration before measurement. Field-emission-gun scanning electron microscopy (FEG-SEM) was performed using a SU-70 Hitachi FEG-SEM instrument (with an accelerating voltage of 5 keV). The sample was prepared by crushing the crystals with an agate mortar and pestle, then stick on the conductive carbon adhesive tapes on aluminum stubs, covered with a thin layer of gold (thickness: ~ 10 nm) using a plasma-sputtering coater.

Electrochemical characterization. Electrochemical behavior of the PBA cathodes was tested in 2032-type coin cells. A Swagelok cell was used for readily recovering the powder for a given e*x-situ* characterization. The cathode electrode disk was prepared by a slurry coated on Al as current collector. 70 wt% active material with 20 wt% carbon Super P (Csp) as conducting agent and 10 wt% Poly(vinylidene fluoride-co-hexafluoropropylene) (PVDF-HFP) were mixed in N-Methyl-2-pyrrolidone (NMP) to obtain a slurry, which was then evenly coated on Al surface and vacuum dried at 100 °C for 10h. The solid concentration of the slurry is around 33 wt%. Each Al disk (1.33 cm^2) was loaded with about 5.5 mg of active material. For the Swagelok cell, cathode powder was prepared by mixing 70 wt% with 30 wt% Csp. The half-cells were then fabricated in an Ar-filled glovebox, with sodium foil as the anode and two Whatman GF/D borosilicate glass fiber sheet as the separator. 1M $NaPF_6$ in PC was used as electrolyte. Full cell was fabricated in the same way except using hard carbon (mass loading: 2 mg cm^{-2}) as anode. Galvanostatic charge/discharge tests were employed for cycling the half and full cells.

Magic angle spinning-nuclear magnetic resonance. *Ex situ* solid-state NMR (SS-NMR) spectra were recorded for ^{1}H and ^{23}Na. The powder cathode samples were cycled to the desired state of charge within

Swagelok cells and then recovered, washed with DMC 3 times then dried under reduced pressure overnight. The sample transfer from the glovebox to the SS-NMR rotors was always done under Argon to avoid air contact, with rotor containing between 1.8 and 2.2 mg of electrode material. The SS-NMR spectra were recorded on a Bruker 4.7 T Avance III HD wide-bore spectrometer operating at 200 MHz for ^{1}H and 52.9 MHz for ^{23}Na, using a 1.3 mm double resonance probe tuned to ^{1}H and ^{23}Na. The rotors were spinning at MAS speeds between 60 and 62 kHz, under nitrogen gas. The recycle delays were set at 1 ms for ^{1}H and 30 ms for ^{23}Na to reduce the contribution of slow relaxing species outside the battery materials (adsorbed water or ions), and Hahn echo sequences were used with echo durations of 2 rotor periods, RF fields amplitudes of 250 kHz for ^{1}H and 150 kHz for ^{23}Na, and 10240 and 20480 transients were recorded for ^{1}H and ^{23}Na, respectively. Chemical shifts were referenced with 1M NaCl in water at 0 ppm for ^{23}Na, and TMS for ^{1}H. The ^{1}H *ex situ* spectra were obtained after subtracting a baseline recorded for an empty rotor in the same conditions. No meaningful ^{1}H SS-NMR signal was detected for D-NaMnHCF, whereas significant ^{1}H signal was detected for H-NaMnHCF. The spectra were analyzed using Bruker's proprietary program Topspin 4.0.

EQCM Analysis. A thin NaMnHCF layer was spray-coated on the gold-patterned 9 MHz Bio-Logic® QCM resonators, using a dedicated mask. Specifically, a diluted slurry (5 mg mL^{-1}) was prepared which was composed of H-NaMnHCF: Csp: PVDF-HFP mixture (63: 27: 10 wt%) in NMP. The resulting slurry was ultrasonicated for at least 15 min to ensure homogenous particle dispersion. The QCM resonators were kept at 100 ˚C during the spray-coating of the slurry with an air-gun. Then, the coated QCM electrode was treated at 100 °C in vacuum for 2h in BUCHI, for the H-NaMnHCF QCM electrodes, whereas to obtain D-NaMnHCF QCM electrode, a further treatment at 150 °C for 5h under 10^{-6} bar vacuum pressure was needed. The mass loading of these QCM electrodes is ~10-11 μg. A lab-developed air-tight EQCM battery cell[36] was mounted in a glove-box in which modified QCM electrode was used as cathode, Na metal as counter and reference electrode, in an electrolyte of 1M $NaPF_6$ in PC. The EQCM with motional resistance monitoring (EQCM-R) was performed outside the glove-box, using a Biologic SP200 work station coupled with a SEIKO QCM922A microbalance which permitted the resonance frequency (f) along with the motional resistance (R_m) to be monitored. All the measurement was conducted using cycling voltammetry (2.5 – 4V *vs.* Na^+/Na, with a scan rate of 0.1 mV s^{-1}), and frequency and motional resistance response of QCM electrode was simultaneously measured, in a temperature controlled oven set to 25 °C. The frequency variation (Δf) is converted to the mass change (Δm) using well-known Sauerbrey equation,[37] $\Delta f = -k_s . \Delta m$, where, $k_s = 16.31 \times 10^7\ \mathrm{Hz\ g^{-1}cm^2}$, is the experimental sensitivity coefficient. The mass per electron (M.P.E.) is estimated by

$\frac{M.P.E.}{n} = \mathrm{F}\frac{\mathrm{D}m}{\mathrm{D}Q}$ (n, number of electrons transferred and F, Faraday's number) and ΔQ is charge calculated from the CV curves.

Operando IR-FOEWS. The operando infrared fibre optic evanescent wave spectroscopy (IR-FOEWS) was conducted using a Fourier-transformed infrared spectrometer (T37 or Invenio S, Bruker), equipped with an accessory system to focus the infrared beam onto one end of the fibre. A mercury-cadmium-tellurium detector, cooled with liquid nitrogen, was used to capture signals in the 12,000 – 600 cm^{-1} range. The fibre was connected to both the light source and detector using a bare fibre terminator and multimode configuration, with a signal amplitude around 10,000 for a 150 µm $Te_2As_3Se_3$ (TAS) fibre. IR-FOEWS spectra were acquired with 16 scans at a 4 cm^{-1} resolution, taking 4 seconds per scan and recorded every 120 seconds.

The operando IR-FOEWS cell assembly was completed in a nitrogen-filled glovebox. A homemade Swagelok cell was modified with a groove drilled into the bottom, serving as the current collector. A TAS fiber was connected to the spectrometer for background measurements, then placed inside the groove and secured with epoxy on both sides, and cured for 12h. This aims to protect the TAS fiber from damage during assembly, and epoxy sealing ensures an air tight environment and maintains cell integrity during operation. A slurry made of 70% active materials and 30% Csp in acetonitrile (ACN) solvent was prepared and was drop cast around the fiber to ensure good adhesion. After the ACN was evaporated, two glass fiber separators soaked in 1M $NaPF_6$ in PC electrolyte were placed over the cathode, and the cell was completed using sodium metal as the anode. The cell was cycled at C/10 for 2 times, the IR spectra were simultaneously collected.

18650 Na-ion cells. Experimental details given above for the full cell configuration was adapted for 18650 cells. First of all, 74 wt% H-NaMnHCF, 21 wt% Csp, and 5 wt% PVDF were well mixed overnight in a Turbula® 3D shaker mixer. Then, a slurry was prepared adding NMP solvent to the previous mixture, with a solid content of 31wt%. After mechanical stirring for 6h, the slurry was coated on an aluminum current collector (by a coating machine (People & Technology Inc. model PDL-250)) then went through two built-in drying chambers set to 80 ˚C and 95 ˚C, respectively, to remove the solvent. The resulting cathode was calendared under 60 °C with optimized pressure to achieve a porosity of around 45%, then cut into pieces with the following dimensions of 5.5 cm x 61.6 cm. This electrode can be stored in the H-NaMnHCF form without extra care. Right before the cell assembly, the cathode was dehydrated at 150°C for 20 h to obtain D-NaMnHCF. The active material content in double coated cathode is 11-12 mg cm^{-2}. With a similar protocol, the anode was prepared using 94 wt% HC, 3 wt% Csp and 3 wt% PVDF for electrode fabrication on an Al current

collector. Then it is cut into pieces with the following dimensions 6 cm x 65 cm and active material mass loading of 5 - 6 mg cm^{-2}. It noted that the dimension of anode is larger than cathode to fabricate well-aligned electrode pairs. All these steps regarding the HC were carried out under ambient conditions.

The 18650 assembly using the D-NaMnHCF cathode and HC anode with the polypropylene ceramic separator (Gelon, width: 60mm, thickness: PP 16 µm + ceramic Al_2O_3 4 µm) was carried out in a dry room (~ dew point -50 °C, 38.8 ppm H_2O). The D-NaMnHCF cathode was further calendared under 90°C to decrease the porosity from 45% to 35%. All the further steps include: winding, placing in the can, spot welding the tab with the can, grooving, welding the cap, electrolyte filling, crimping and hermetically sealing of the cell with epoxy (cured for 12h). The D-NaMnHCF//HC 18650 cells were settled for 1 day for electrolyte impregnation. The active mass ratio of D-NaMnHCF//HC was fixed as 2 (capacity ratio of Negative/Positive electrode is 1.1) based on several optimizations. 1M $NaPF_6$ in EC/PC/DMC = 1:1:2 (in volume) was used as electrolyte. Due to the separator wettability issues with PC, we switched to EC : PC : DMC for the 18650 cells, which delivered better % nominal (original) capacity retention with increased C-rate (**Figure S19**). A formation cycle at C/20 was performed before further cycling. A matrix with constant current and constant voltage (CCCV) were carried out during cycling sequence. Specifically, the cell was charged with set constant current to the cut off voltage at 3.8 V and undergoes a constant voltage step until the current reaches to C/20, which was followed by the regular discharge.[38]

Acknowledgements

ZL thanks China Scholarship Council for the financial support of her PhD thesis. TIAMAT Energy, France is gratefully acknowledged for providing the HC anodes designed for R&D purposes for the 18650 and coin cell studies. The authors thank Erik Elkaïm at CRISTAL beamline for the synchrotron XRD measurements at SOLEIL, France. The authors acknowledge R. Chometon, E. Grepin and A. Chaupatnaik (Collège de France) for their help with the SEM, TGA/DSC and ICP-MS analyses. The author thanks S. Mariyappan, J. Forero-Saboya and R. Demir-Cakan for their valuable comments and discussions.

Associated content

Further structural, morphological and compositional analyses of the AP-NaMnHCF, H-NaMnHCF and D-NaMnHCF samples; additional electrochemical tests, electrogravimetric analysis details, *ex*-situ solid state

NMR, as well as tables presenting compositional and structural data (ICP-MS and Rietveld refinement results).

Conflict of interest

Authors declare no conflict of interest.

Data Availability Statement

The data that support the findings of this study are available from the corresponding author upon reasonable request.

References

1. Hasa, I.; Mariyappan, S.; Saurel, D.; Adelhelm, P.; Koposov, A. Y.; Masquelier, C.; Croguennec, L.; Casas-Cabanas, M., Challenges of today for Na-based batteries of the future: From materials to cell metrics. *Journal of Power Sources* **2021,** *482*, 228872.
2. Patnaik, S. G.; Adelhelm, P., Prussian Blue Electrodes for Sodium-Ion Batteries. In *Sodium-Ion Batteries*, 2022; pp 167-187.
3. Wu, C.; Yang, Y.; Zhang, Y.; Xu, H.; He, X.; Wu, X.; Chou, S., Hard carbon for sodium-ion batteries: progress, strategies and future perspective. *Chemical Science* **2024,** *15* (17), 6244-6268.
4. Hurlbutt, K.; Wheeler, S.; Capone, I.; Pasta, M., Prussian Blue Analogs as Battery Materials. *Joule* **2018,** *2* (10), 1950-1960.
5. Qian, J.; Wu, C.; Cao, Y.; Ma, Z.; Huang, Y.; Ai, X.; Yang, H., Prussian Blue Cathode Materials for Sodium-Ion Batteries and Other Ion Batteries. *Adv. Energy Mater.* **2018,** *8* (17), 1702619.
6. Wang, W.; Hu, Z.; Yan, Z.; Peng, J.; Chen, M.; Lai, W.; Gu, Q.-F.; Chou, S.-L.; Liu, H.-K.; Dou, S.-X., Understanding rhombohedral iron hexacyanoferrate with three different sodium positions for high power and long stability sodium-ion battery. *Energy Storage Materials* **2020,** *30*, 42-51.
7. Peng, J.; Gao, Y.; Zhang, H.; Liu, Z.; Zhang, W.; Li, L.; Qiao, Y.; Yang, W.; Wang, J.; Dou, S.; Chou, S., Ball Milling Solid-State Synthesis of Highly Crystalline Prussian Blue Analogue Na2−xMnFe(CN)6 Cathodes for All-Climate Sodium-Ion Batteries. *Angew. Chem. Int. Ed.* **2022,** *61* (32), e202205867.
8. Xu, Z.; Sun, Y.; Xie, J.; Nie, Y.; Xu, X.; Tu, J.; Zhang, J.; Qiu, L.; Zhu, T.; Zhao, X., Scalable Preparation of Mn/Ni Binary Prussian Blue as Sustainable Cathode for Harsh-Condition-Tolerant Sodium-Ion Batteries. *ACS Sustainable Chemistry & Engineering* **2022,** *10* (40), 13277-13287.
9. Bauer, A.; Song, J.; Vail, S.; Pan, W.; Barker, J.; Lu, Y., The Scale-up and Commercialization of Nonaqueous Na-Ion Battery Technologies. *Adv. Energy Mater.* **2018,** *8* (17), 1702869.

10. Ma, X.-H.; Wei, Y.-Y.; Wu, Y.-D.; Wang, J.; Jia, W.; Zhou, J.-H.; Zi, Z.-F.; Dai, J.-M., High crystalline Na2Ni[Fe(CN)6] particles for a high-stability and low-temperature sodium-ion batteries cathode. *Electrochimica Acta* **2019,** *297*, 392-397.
11. Adil, M.; Sau, S.; Dammala, P.; Mitra, S., Comprehensive Study of Sodium Copper Hexacyanoferrate, as a Sodium-Rich Low-Cost Positive Electrode for Sodium-Ion Batteries. *Energy & Fuels* **2022,** *36* (14), 7816-7828.
12. Wessells, C. D.; Peddada, S. V.; McDowell, M. T.; Huggins, R. A.; Cui, Y., The Effect of Insertion Species on Nanostructured Open Framework Hexacyanoferrate Battery Electrodes. *Journal of The Electrochemical Society* **2011,** *159* (2), A98.
13. Oliver-Tolentino, M.; Ramos-Sánchez, G.; Guzmán, G.; Avila, M.; González, I.; Reguera, E., Water effect on sodium mobility in zinc hexacyanoferrate during charge/discharge processes in sodium ion-based battery. *Solid State Ionics* **2017,** *312*, 67-72.
14. Matsuda, T.; Takachi, M.; Moritomo, Y., A sodium manganese ferrocyanide thin film for Na-ion batteries. *Chemical Communications* **2013,** *49* (27), 2750-2752.
15. Brant, W. R.; Mogensen, R.; Colbin, S.; Ojwang, D. O.; Schmid, S.; Häggström, L.; Ericsson, T.; Jaworski, A.; Pell, A. J.; Younesi, R., Selective Control of Composition in Prussian White for Enhanced Material Properties. *Chemistry of Materials* **2019,** *31* (18), 7203-7211.
16. Shao, T.; Li, C.; Liu, C.; Deng, W.; Wang, W.; Xue, M.; Li, R., Electrolyte regulation enhances the stability of Prussian blue analogues in aqueous Na-ion storage. *J. Mater. Chem. A* **2019,** *7* (4), 1749-1755.
17. Song, J.; Wang, L.; Lu, Y.; Liu, J.; Guo, B.; Xiao, P.; Lee, J. J.; Yang, X. Q.; Henkelman, G.; Goodenough, J. B., Removal of interstitial H2O in hexacyanometallates for a superior cathode of a sodium-ion battery. *J Am Chem Soc* **2015,** *137* (7), 2658-64.
18. Liu, X.; Zhao, J.; Dong, H.; Zhang, L.; Zhang, H.; Gao, Y.; Zhou, X.; Zhang, L.; Li, L.; Liu, Y.; Chou, S.; Lai, W.; Zhang, C.; Chou, S., Sodium Difluoro(oxalato)borate Additive‐Induced Robust SEI and CEI Layers Enable Dendrite‐Free and Long‐Cycling Sodium‐Ion Batteries. *Adv. Funct. Mater.* **2024**.
19. Herren, F.; Fischer, P.; Ludi, A.; Haelg, W., Neutron diffraction study of Prussian Blue, Fe4[Fe(CN)6]3.xH2O. Location of water molecules and long-range magnetic order. *Inorganic Chemistry* **1980,** *19* (4), 956-959.
20. Dreyer, S. L.; Maddar, F. M.; Kondrakov, A.; Janek, J.; Hasa, I.; Brezesinski, T., Elucidating Gas Evolution of Prussian White Cathodes for Sodium-ion Battery Application: The Effect of Electrolyte and Moisture. **2024,** *7* (4), e202300595.
21. O'dell, L.; Kourati, D.; Salager, E.; Forsyth, M.; Deschamps, M., Understanding sodium battery materials using high-field solid-state nuclear magnetic resonance spectroscopy. **2022,** *6*, 39-44.
22. Bendadesse, E.; Gervillié-Mouravieff, C.; Leau, C.; Goloviznina, K.; Rabuel, F.; Salanne, M.; Tarascon, J.-M.; Sel, O., Spotting Interface Structuring during Na-Insertion into the NaSICON Na3V2(PO4)3 by EQCM and Operando Fiber Optic Infrared Spectroscopy. *Adv. Energy Mater.* **2023,** *13* (26), 2300930.
23. Gervillié-Mouravieff, C.; Boussard-Plédel, C.; Huang, J.; Leau, C.; Blanquer, L. A.; Yahia, M. B.; Doublet, M. L.; Boles, S. T.; Zhang, X. H.; Adam, J. L.; Tarascon, J. M., Unlocking cell chemistry evolution with operando fibre optic infrared spectroscopy in commercial Na(Li)-ion batteries. *Nature Energy* **2022,** *7* (12), 1157-1169.
24. Song, J.; Wang, L.; Lu, Y.; Liu, J.; Guo, B.; Xiao, P.; Lee, J. J.; Yang, X. Q.; Henkelman, G.; Goodenough, J. B., Removal of interstitial H2O in hexacyanometallates for a

superior cathode of a sodium-ion battery. *Journal of the American Chemical Society* **2015,** *137* (7), 2658-64.
25. He, Y.; Dreyer, S. L.; Akçay, T.; Diemant, T.; Mönig, R.; Ma, Y.; Tang, Y.; Wang, H.; Lin, J.; Schweidler, S.; Fichtner, M.; Hahn, H.; Brezesinski, T.; Breitung, B.; Ma, Y., Leveraging Entropy and Crystal Structure Engineering in Prussian Blue Analogue Cathodes for Advancing Sodium-Ion Batteries. *ACS Nano* **2024**.
26. Xu, C.; Ma, Y.; Zhao, J.; Zhang, P.; Chen, Z.; Yang, C.; Liu, H.; Hu, Y. S., Surface Engineering Stabilizes Rhombohedral Sodium Manganese Hexacyanoferrates for High-Energy Na-Ion Batteries. *Angew Chem Int Ed Engl* **2023,** *62* (13), e202217761.
27. Subasinghe, L. U.; Satyanarayana Reddy, G.; Rudola, A.; Balaya, P., Analysis of Heat Generation and Impedance Characteristics of Prussian Blue Analogue Cathode-based 18650-type Sodium-ion Cells. *Journal of The Electrochemical Society* **2020,** *167* (11), 110504.
28. Wu, X.; Wu, C.; Wei, C.; Hu, L.; Qian, J.; Cao, Y.; Ai, X.; Wang, J.; Yang, H., Highly Crystallized Na2CoFe(CN)6 with Suppressed Lattice Defects as Superior Cathode Material for Sodium-Ion Batteries. *ACS Applied Materials & Interfaces* **2016,** *8* (8), 5393-5399.
29. Maddar, F. M.; Walker, D.; Chamberlain, T. W.; Compton, J.; Menon, A. S.; Copley, M.; Hasa, I., Understanding dehydration of Prussian white: from material to aqueous processed composite electrodes for sodium-ion battery application. *J. Mater. Chem. A* **2023,** *11* (29), 15778-15791.
30. Wang, W.; Gang, Y.; Peng, J.; Hu, Z.; Yan, Z.; Lai, W.; Zhu, Y.; Appadoo, D.; Ye, M.; Cao, Y.; Gu, Q.-F.; Liu, H.-K.; Dou, S.-X.; Chou, S.-L., Effect of Eliminating Water in Prussian Blue Cathode for Sodium-Ion Batteries. *Adv. Funct. Mater.* **2022,** *n/a* (n/a), 2111727.
31. Huang, Y.; Zhang, X.; Ji, L.; Wang, L.; Xu, B. B.; Shahzad, M. W.; Tang, Y.; Zhu, Y.; Yan, M.; Sun, G.; Jiang, Y., Boosting the sodium storage performance of Prussian blue analogs by single-crystal and high-entropy approach. *Energy Storage Materials* **2023,** *58*, 1-8.
32. Li, Z.; Lou, X.; Kang, S.; Liu, D.; Geng, F.; Shen, M.; Hu, B., In-cell dehydration of sodium manganese hexacyanoferrate cathode revealed by solid-state NMR. *Magnetic Resonance Letters* **2024**, 200135.
33. Niwa, H.; Moriya, T.; Shibata, T.; Fukuzumi, Y.; Moritomo, Y., In situ IR spectroscopy during oxidation process of cobalt Prussian blue analogues. *Scientific Reports* **2021,** *11* (1), 4119.
34. Wu, J.; Song, J.; Dai, K.; Zhuo, Z.; Wray, L. A.; Liu, G.; Shen, Z.-x.; Zeng, R.; Lu, Y.; Yang, W., Modification of Transition-Metal Redox by Interstitial Water in Hexacyanometalate Electrodes for Sodium-Ion Batteries. *Journal of the American Chemical Society* **2017,** *139* (50), 18358-18364.
35. Rudola, A.; Du, K.; Balaya, P., Monoclinic Sodium Iron Hexacyanoferrate Cathode and Non-Flammable Glyme-Based Electrolyte for Inexpensive Sodium-Ion Batteries. *Journal of The Electrochemical Society* **2017,** *164* (6), A1098.
36. Lemaire, P.; Dargon, T.; Alves Dalla Corte, D.; Sel, O.; Perrot, H.; Tarascon, J.-M., Making Advanced Electrogravimetry as an Affordable Analytical Tool for Battery Interface Characterization. *Analytical Chemistry* **2020,** *92* (20), 13803-13812.
37. Sauerbrey, G., Verwendung von Schwingquarzen zur Wägung dünner Schichten und zur Mikrowägung. *Zeitschrift für Physik* **1959,** *155* (2), 206-222.
38. Thompson, L. M.; Harlow, J. E.; Eldesoky, A.; Bauer, M. K. G.; Cheng, J. H.; Stone, W. S.; Taskovic, T.; McFarlane, C. R. M.; Dahn, J. R., Study of Electrolyte and Electrode Composition Changes vs Time in Aged Li-Ion Cells. *Journal of The Electrochemical Society* **2021,** *168* (2).